"The Feasibility of a Cochlear Nucleus Auditory Prosthesis Based on Microstimulation"

Contract No. NO1-DC-5-2105

QUARTERLY PROGRESS REPORT #4

April 1, 1996 to June 30, 1996

HOUSE EAR INSTITUTE

2100 W. Third St.
Los Angeles, CA 90057

R.V. Shannon, Ph.D.
J. Moore, Ph.D.
J. Huang, B.S.
F. Portillo, B.S.E.
B. Wu, B.S.

HUNTINGTON MEDICAL RESEARCH INSTITUTES

Neurological Research Laboratory
734 Fairmount Ave
Pasadena, CA 91105

D.B. McCreery, Ph.D.
W.F. Agnew, Ph.D.
T.G.H. Yuen, Ph.D.
L.A. Bullara, B.S.

TABLE OF CONTENTS

1.0 Introduction

This report describes work done at the House Ear Institute (HEI) under contract N01-DC-5-2105, "Feasibility of a Cochlear Nucleus Auditory Prosthesis Based on Microstimulation". The overall goal of the contract is to determine the feasibility of a prosthetic device to achieve multiple electrode tonotopic stimulation of the human cochlear nucleus. The application of such a prosthesis would be primarily in patients with no auditory nerve, usually as a result of bilateral vestibular schwannomas (VS). The portions of the contract performed at HEI are focused on work with human material. One goal is to determine the status and structure of the residual cochlear nuclear complex following VS removal and its implications for the design of the penetrating electrode system. Another goal is to devise methods for delivering the microelectrode system into a human brainstem through the surgical approach used for tumor removal. Three projects will be described: (1) anatomical studies of the shape and location of the human cochlear nuclear complex relative to brainstem surface landmarks in normal subjects and patients with VS (Section 2), (2) anatomical/mechanical studies leading to the design of a surgical insertion tool (Section 3), and (3) force measurements of insertions of sample electrodes into fresh human brainstem material (Section 4).

2.0 Design of a Cochlear Nucleus Electrode Array

The currently used brainstem surface electrode array is placed within the lateral recess of the fourth ventricle, where it is situated lateral to the dorsal cochlear nucleus (DCN) and caudal to the ventral cochlear nucleus (VCN). In the case of an penetrating microelectrode which would target the VCN, the question arises as to whether the surface of the brainstem provides any visible landmarks to guide the surgeon in placement of the device. In other words, is it possible to identify the location of the human cochlear nuclei on the basis of brainstem surface features? To answer this question, we are currently correlating the location of brainstem surface features with that of deeper nuclei in the region of the pontomedullary junction. Since previous work (QPR #8, Contract 1989-92) indicated that the cochlear nuclear complex is reduced in size in subjects with acoustic neuromas, these studies are being carried out in the brainstems of normal subjects and subjects with unilateral or bilateral eighth nerve tumors.

Transverse (axial) views of brainstem sections are seen in Figures 2.1 and 2.2. The sections are taken from the brainstem of a normal subject who was 46 years old at the time of death. In Figure 2.1, the more caudal plane of section, the positions of the dorsal cochlear nucleus and pontobulbar nucleus are illustrated. In the color version of the figure, the cochlear nuclear complex is represented in red and the pontobulbar nucleus in blue. For each structure, broken lines indicate the extent of its profile, or projection, onto the brainstem surface. Anatomical

structures are designated as follows: cst = cerebrospinal tract; floc = flocculus of cerebellum; icp = inferior cerebellar peduncle; io = inferior olive; lvn = lateral vestibular nucleus; mvn = medial vestibular nucleus; pbn = pontobulbar nucleus; pn = pontine nuclei; tb = trapezoid body, VII = facial nerve; VIII = vestibulocochlear nerve. Two anatomical points are obvious from this illustration. First, the pontobulbar nucleus is an irregularly shaped cell mass which lies near the ventral brainstem surface, superficial to the cochlear nuclei. Thus any penetrating electrode array will pass through the pontobulbar nuclei before reaching the cochlear nuclei. Secondly, an electrode passing through the surface area overlying the dorsal cochlear nucleus will not necessarily lie entirely within the nucleus, which is extremely narrow and arches from ventrolateral to dorsomedial.

A more rostral section through the brainstem and cochlear nuclear complex of the normal subject is represented in Figure 2.2 (colors and abbreviations as in Fig. 2.1). The pontobulbar nucleus lies just beneath the brainstem surface, and the ventral cochlear nucleus is situated deeper. At this level, both the seventh and eighth nerves can be seen on the brainstem surface. An appropriately scaled multielectrode device is illustrated near the brainstem. From this figure, it is obvious that an electrode inserted through the eighth nerve root would, if appropriately angled, enter the VCN at some depth below the surface.

Similar schematic drawings were made from a series of evenly spaced transverse sections, approximately every 600 μm, through the cochlear nuclear complex in three other subjects. These included two subjects with unilateral neuromas (89-54 and 92-01) and one subject with resected bilateral acoustic neuromas caused by neurofibromatosis, type 2 (NF2, 92-13). In all three cases, the eighth nerve tumors had been surgically resected. The NF2 subject had received an auditory brainstem implant at the time of the second surgery. From each series of transverse brainstem sections, a three-dimensional reconstruction was created to view the brainstem surface from its ventral aspect, i.e., the point of view of the surgeon. Figures 2.3, 2.4 and 2.5 illustrate these schematic views of the brainstem surface: all figures have been oriented to appear as the right side of the brainstem. In each case, the upper portion of the figure illustrates the seventh and eighth nerve roots, which are the only features visible on the brainstem surface. The lower half of the figure illustrates the nerve roots superimposed on the underlying (and thus invisible) pontobulbar nucleus and cochlear nuclei. A dashed line indicates the position of the brainstem midline, and a curved line indicates the edge of the ventrally extending core of the brainstem.

In the normal subject (Fig. 2.3), both nerve roots are identifiable on the brainstem surface. The pontobulbar nuclei are extensive, and extend quite far rostral to the cochlear nuclear complex. The vestibulocochlear nerve root overlies the anterior half of the VCN, while the facial nerve root lies caudal and medial to the CN. In the two subjects with unilateral acoustic neuromas (Fig. 2.4), the

diagrammatic representations show possible variations in the configuration of the eighth nerve root. In the subject on the left side of the figure, a facial nerve root is present but no eighth nerve root can be identified. In the subject on the right side, there is a separation of the vestibular and cochlear portions of the nerve at the point where they enter the brainstem, but the cochlear nerve root overlies the anterior VCN, as in the normal subject. These two subjects also illustrate the variability in the development of the pontobulbar nuclei, which are extremely small in the subject on the left and not present in the subject on the right. The final figure (Fig. 2.5) represents the two sides of the brainstem in the subject with neurofibromatosis. in this subject the pontobulbar nuclei are moderately large and partially cover the cochlear nuclei. On one side, only a facial nerve root is present, situated rostral and medial to the VCN. On the opposite side of the brainstem, both seventh and eighth nerve roots are present but the seventh nerve root is located relatively far medial to the VCN.

Even with this limited number of cases (four subjects, five CNs), some tentative conclusions can been drawn. The facial nerve root is present in all cases in this series, but it is not consistent in its position relative to the VCN. This casts some doubt on the possibility of using the seventh nerve as a reliable landmark for electrode insertion. The lateral, or cochlear, portion of eighth nerve root consistently overlies the anterior VCN, making it an excellent landmark for electrode insertion, but the entire eighth nerve root is not present in two out of five cases, i.e., in 40% of the cases studied to date. Absence of a remnant of the eighth nerve generally indicates that the entire nerve was involved by the schwannoma and was resected at the time of surgery.

A number of questions remain to be answered. First, if the eighth nerve root is to be used as a landmark for inserting a microelectrode array, can an electrode array penetrate the tough pial-glial neurolemmal covering of the nerve root? This issue has been investigated in the series of insertion force studies, and is discussed in Section 4.0 of this report. Secondly, will a linear array of electrodes, once inserted, cross the tonotopic planes of the VCN? This issue will be dealt with in the coming months by computer simulation of insertion of electrode arrays of various lengths and configurations through the eighth nerve root. Third, given that insertion through the nerve root will place an electrode array in the anterior VCN, will stimulation here allow speech perception? There are previous reports (D. McCreery and H. El Kashlan, personal communications) that stimulation of the anterior VCN is less effective in stimulating the inferior colliculus than stimulation in the posterior VCN. A difference between the two portions of the VCN in their effect on collicular activity is a reasonable possibility, since much of the projection from the anterior VCN is directed into the medial and lateral olivary nuclei. At the level of the olivary nuclei, information on stimulus interaural differences is extracted (Yin and Chan, 1990; Tsuchitani and Johnson, 1991) and relayed to the inferior colliculus (Brunso-Bechtold et al., 1981; Adams, 1983; Henkel and Spangler, 1983; Shneiderman and Henkel, 1987). The neural

processing in the olivary nuclei is believed to function in spatial localization of stimuli, and may not be useful for speech perception. Because of this issue, the efficacy of anterior VCN stimulation at the level of the inferior colliculus is being addressed in animal stimulation-recording experiments, carried out jointly by investigators at HMRI and HEI. Results of these studies will be detailed in future quarterly progress reports.

3.0 Design of an Insertion Tool

The first tool design was developed using a generic head model, to which we added a reconstruction of the brainstem auditory nuclei and surrounding structures. The first tool mockup was tested in cadaver heads with traslabyrinthine surgical openings. Both of these testing methods, however, have limitations. In the cadaver head, as in the surgical patient, there is no way to visualize the cochlear nuclei, and thus no way to judge if the tool is aligned at the correct angle to penetrate the VCN and cross its tonotopic planes. In the computerized head model, the skull module is highly accurate in its depiction of the external skull surface, but it does not include the internal bony surface or dural structures such as the tentorium, or sigmoid sinus, or jugular vein. As reported in QPR #2 of this contract, we have attempted to achieve greater accuracy by digitizing 24 CT scans through the midbrainstem region. These radiological images include internal features of the surgical opening, including the petrous wing of the temporal bone, the dura, and venous sinuses.

Figure 3.1 illustrates the digitized CT images fitted into the generic skull. One basis for combining the two three-dimensional computer images is to determine if external landmarks might be used as reference points by the surgeon. In the color version of this figure, bone surrounding the translabyrinthine opening is represented in blue and dural structures in yellow. A view of this composite model in the horizontal plane is shown in Figure 3.2. In this wireframe reconstruction, the digitized CT sections are fitted into the right half of the generic head and skull. In the color version, the skull is represented in blue, the dura and enclosed venous structures in yellow, the eighth nerve, cochlear nuclei and trapezoid body in red, the trigeminal nerve in green, the facial nucleus and nerve in blue, and the vestibular nuclei in green. The insertion tool (in aqua) can be seen to pass through the surgical opening in the skull and to bend at an angle of approximately 50°. This angle allows the tip to contact the brainstem surface near the entrance of the eighth nerve.

A higher power view of the regions surrounding the end of the tool is shown in Figure 3.3. As in Figure 3.2, all auditory structures are represented in red. This view demonstrates that the tool passes over the apex of the petrous pyramid and under the tentorium. The end of the tool is directed toward the VCN

at an angle that would allow an electrode array ejected from the tip to cross the VCN orthogonal to its tonotopic planes (three planes represented in black).

As a final determination of the position of the electrode, the figure shown in Figure 3.3 was rotated to a lateral view, and the wire frame image was converted to a solid surface figure. In this view (Fig. 3.4), the insertion tool (in aqua) can be seen to pass through the opening between the bone anterior to the dural channel forming the sigmoid sinus (in yellow). This figure illustrates that movement of the tool is mainly limited to rotation about the axis of its handle, as motion in any other plane will be restricted by the bony structures or dura.

Based on these three-dimensional computer reconstructions, a prototype insertion tool is presently being fabricated by Altair Instruments. Several prototype instruments will be fabricated and evaluated by William Hitselberger for suitable handling properties under surgical conditions.

4.0 Insertion Force Measurements

The human cochlear nucleus is covered by a tough pial-glial layer that presents a difficult barrier for penetrating microelectrodes. Electrodes must be sharp enough to penetrate this tough layer and must be inserted with force sufficient to ensure penetration, while causing minimal trauma to potentially stimulable tissues and vasculature. We have measured the force required to insert penetrating microelectrodes through the pial layer into the underlying cochlear nucleus in unfixed human brainstem material. We have designed a computer-controlled mechanical insertion device to control the insertion speed and to record the actual forces necessary for penetrating the pial layer with different types of microelectrodes.

Equipment. A computer-controlled apparatus was constructed to advance microelectrodes into tissue, with precise control of velocity and acceleration. A precision stepper motor controlled the position and velocity profile of an electrode carrier. Actual position of the electrode carrier was independently measured by a position-to-voltage converter. The voltage was digitized at the rate of one sample every 20 ms and stored in a file for later analysis. Similarly, force was measured by a strain gauge mounted in the electrode carrier, which converted force into voltage. The force-voltage was digitized at 50 Hz and stored in a file for later analysis. Penetration velocities of 12.7, 25.4, and 76.2 mm/sec were tested. At high speeds the apparatus produced vibration when accelerating and decelerating. The acceleration/deceleration profile was smoothed to eliminate most of the vibration so that it did not obscure the force recordings.

Electrodes: Overall, seven electrode types were evaluated:

1. **Ir3**. Iridium shaft, sharp tip: 75 μm shaft of Iridium wire, insulated with Epoxylite electrode varnish. Tip etched to cone with 3 μm tip diameter.

2. **Ir12.** Iridium shaft, blunt tip: same as #1, but with 12 μm diameter tip.

3. **Si.** Silicon Probe alone: University of Michigan photolithographic probe, 100 μm wide blade, 3.5 mm long with a sharp tip produced by shallow Boron diffusion etching.

4. **SiIrMDX.** Reinforced Silicon Probe, type 1: same as #3, but glued to HMRI Iridium shaft with MDX 4210 adhesive. The tip of the Iridium shaft protruded 1.0 mm beyond the tip of the silicon probe. Thus, pial-glial layer was first penetrated by the Iridium shaft.

5. **SiIrA.** Reinforced Silicon Probe, type 2: same as #4, but attached with Type A adhesive.

6. **SiIrE**. Reinforced Silicon Probe, type 3: similar to #4, but 4 mm long Silicon probe attached by Epoxylite electrode varnish applied evenly along the Iridium shaft, resulting in a smoother profile along the shaft than electrode #5..

7. **4Ir12**. Arrays of 4 iridium shafts: 2, 3, 4 and 5 mm long, each insulated with Epoxylite electrode varnish and with 12 μm tip diameters, arranged at the vertices of a square with sides 400 μm apart.

Figure 4.1 shows photographs of three electrodes mounted for testing in the apparatus to measure penetration forces. The upper panel (4.1A) shows electrode type Ir3: a single Iridium 75 μm diameter shaft with a 3 μm tip. The middle panel (4.1B) shows electrode type SiIrE: the Silicon photolithographic blade mounted on an Iridium shaft with Epoxylite electrode varnish. The lower panel (4.1C) shows electrode type 4Ir12, the four-shaft array of blunt Iridium electrodes.

Tissue. Human brainstems were obtained from the National Disease Research Institute and from the HEI Temporal Bone Bank with the assistance of Dr. Fred Linthicum. They were fresh, unfixed specimens tested for communicable diseases.

The first two specimens were simply mounted unsupported on a platform, which resulted in conditions during experimental insertions that did not reflect conditions to be expected during clinical implantation of such electrode arrays. In these cases the electrode force applied to the pial layer resulted in displacement of the brainstem away from the electrode. This condition would not occur in clinical

application because the brainstem would be supported by the rest of the brain and skull.

To support the brainsems during insertion, they were imbedded in gelatin and frozen, after partial dissection to expose the region of the cochlear nucleus. Just prior to the insertion testing the specimens were thawed, the gelatin was dissected away from the area of the VII and VIII nerve roots, and the specimens were positioned at the desired angle to the penetrating apparatus to simulate the insertion angle during surgery. Electrodes were positioned so that tissue contact was initiated at the desired velocity and were driven 4-5 mm beyond the initial point of contact, depending on the length of electrode shaft.

Insertions into the last two brainstems were qualitatively and quantitatively different from the insertions into prior brainstems. This may be due to the quality of the tissue samples. In prior brainstems, obtained from the National Disease Research Institute, the tissue remained unfrozen for a considerable period of time before being mounted in gelatin for the experimental penetrations. The last two brainstems were obtained locally and were imbedded in gelatin and frozen quickly, resulting in specimens that were of excellent quality. For this reason we base most of our conclusions about insertion forces on the results with the last two experiments.

Results. The results of all penetration runs for the last three experiments are presented in Tables 4.1, 4.2 and 4.3. Each table lists the electrode type, insertion speed, site of penetration, and the force required for penetration.

Figure 4-2 shows two penetrations of an Iridium HMRI electrode into fresh (unfixed) human brainstem tissue. Each panel shows two traces as a function of time: (1) position of the electrode in mm, and (2) force in grams. The position trace shows the location of the motorized electrode carrier as a function of time and is referenced to the left ordinate. The other trace shows the force measured during the penetration as a function of time and is referenced to the right ordinate.

The top panel (FIG 4.2A) illustrates a successful penetration at a fast insertion speed (76.2 mm/sec) with a blunt-tipped Iridium electrode (Ir12). In this case the electrode penetrated cleanly with minimal tissue dimpling at the time of contact, noted visually. The force record shows a peak force of 4.66 grams and a sudden drop in force corresponding to the penetration of the pial layer. The force record returns quickly to zero, indicating that there are no additional forces on the electrode (such as frictional drag on the sides of the electrode shaft). The oscillation observed was due partly to the vibration of the insertion apparatus from the sudden deceleration of the motor. A similar but smaller oscillation can be seen when the motor starts accelerating at 0.15 sec. These artifactual oscillations are only seen in the traces for the rapid insertion velocities. Force magnitudes were measured prior to the onset of those oscillations.

Figure 4.2B presents results from one trial in which the microelectrode did not penetrate into the tissue: a slow insertion speed (12.7 mm/sec) with a sharp Iridium electrode (Ir3). Note that in this case the force profile shows a peak at the time of initial contact, a slight reduction in force as the tissue yields, and then a static force as the tissue surface dimpled but was not penetrated and presents a constant resistance to the electrode.

In the case of a successful penetration the force rebounds to zero, indicating that there are no remaining resistive forces of the tissue on the electrode or electrode shaft. In the case of an unsuccessful penetration the force decreases slightly, probably due to the elasticity of the tissue itself, but the force does not return to zero. A similar decrease in force was observed with a blunt hypodermic shaft that did not and was not intended to penetrate the pial layer (Table 4.1, penetrations 26 and 27). The remaining static force indicates that the electrode either did not penetrate the pial layer, or incompletely penetrated the pial layer, with a static force acting on the cone of the electrode tip or on the electrode shaft.

Fig. 4.3A presents an example of a penetration of a SiIrE electrode at a medium insertion speed (25.4 mm/sec). Although a high force was required (13.1 grams) the electrode did penetrate the pial layer. The high force required probably reflects the thicker pial layer surrounding the nerve root area, since penetrations in other regions of this same brainstem required low levels of force (see Table 4.3). In this case the initial penetration was by the Iridium shaft supporting the Silicon blade. A secondary peak in the force record can be seen following the initial peak force - indicating the contact of the Silicon electrode tip with the punctured tissue. This implies that once the pial layer is penetrated, even in the tough nerve root region, the Silicon blade can be inserted into the tissue with a minimum of additional force.

Figure 4.3B shows the penetration record for a four-electrode array of Iridium shafts (electrode type 4Ir12) at high speed (76.2 mm/sec). Note the successive small peaks in the force record, indicating the tissue contact and penetration of each electrode shaft in succession.

Silicon electrodes are desirable for ease of manufacture, and also because a large number of stimulable sites can be placed along a single penetrating shaft. However, our initial tests of these electrodes indicated that the unreinforced Silicon blade was not strong enough to penetrate the pial tissue layer. In these electrodes the leading edge of the Silicon blade was sharpened by shallow Boron diffusion etching. We will work with the University of Michigan electrode fabrication facility to design alternative electrodes for the present application that might achieve the desired stiffness. In addition we will attempt to puncture the pial layer prior to insertion, although the feasibility of nontraumatically opening the

pial layer during an actual surgical procedure seems unlikely. Another approach is to reinforce the Silicon blade with a stiffening rib. Electrodes SilrA, SilrMDX, and SilrE all used a HMRI Iridium electrode as a stiffening rib. The Iridium electrode was glued to the back of the Silicon blade with either MDX4210 adhesive, Type A adhesive, or with Epoxylite. The properties of each adhesive and the methods for applying them were such that the Epoxylite had the smoothest surface in the finished composite. The tip of the Iridium shaft was positioned 1 mm ahead of the tip of the Silicon blade. Thus, in this configuration, the Iridium shaft penetrated the pial layer and the Silicon blade followed.

Future Plans. It is desirable to find a technology for stiffening the Silicon shaft that is less labor-intensive and more reliable than the present gluing method. Several designs are possible with laminated Silicon probes, but the tip of the leading blade would have to penetrate the pial layer. Thus, in our next series of penetration force measure we will mount the Silicon blade with it's tip leading the Iridium stiffening rib. The sharpened tip of the Silicon blade will then be examined for integrity before and after insertions into unfixed human brainstems.

In summary, sharp Iridium electrodes (Ir3) penetrated reliably at medium and high penetration speeds, but even sharp electrodes did not penetrate the tough pial layer at low speeds. Blunter electrodes (Ir12) penetrated reliably only at the fastest insertion speed. Peak force required for penetration was similar across all electrodes and insertion speeds at about 4 grams. Higher levels of force were required to penetrate in the nerve root area where the pial layer is thickest. Surface dimpling does not appear to be large enough to pose a risk of serious mechanical trauma. Thus, if blunt electrodes are desirable because they produce less tissue and vascular damage, the insertion tool must be capable of insertion speeds of 76.2 mm/sec or greater to reliably penetrate the pial layer. This high speed increases the complexity of the insertion tool. Our initial experience with Silicon photolithographic arrays was discouraging. Unreinforced Silicon probes broke before they penetrate the pial-glial layer. In the next year we will work with the electrode fabrication facility at the University of Michigan to design prototype Silicon electrodes that may be strong enough for this application.

5.0 References

Adams JC. Ascending projections to the inferior colliculus. J Comp Neurol 183:519-538, 1979

Brunso-Bechtold JK, Thompson GC and Masterton RB. HRP study of the organization of auditory afferents ascending to central nucleus of the inferior colliculus in cat. J Comp Neurol 197:705-722, 1981

Henkel CS and Spangler KM. Organization of the efferent projections of the medial superior olivary nucleus in the cat as revealed by HRP and autoradiographic tracing methods. J Comp Neurol 221:416-428, 1983

Shneiderman A and Henkel CK. Banding of lateral superior olivary nucleus afferents in the inferior colliculus: a possible substrate for sensory integration. J Comp Neurol 266: 519-5324, 1987

Tsuchitani C and Johnson DH. Binaural cues and signal processing in the superior olivary complex. Pp 163-198 in Neurobioloby of Hearing: The Central Auditory System (Eds, Altshculer RA, Bobbin RP, Clopton BM and Hoffman DW). Raven Press, New York, 1991

Yin TCT and Chan JCK. Interaural time sensitivity in medial superior olive of cat. J Neurophysiol 645:465-488, 1990

Penetration Experiment #3 March 19 1996

Insertion	Electrode type	velocity at impact cm/sec	Site of penetration	Penetration	Force in grams
1	Ir3	2.56	Left side	YES (dimple)	3.55
2	Ir3	7.62	Left side	YES (dimple)	3.33
3	Ir3	7.62	Left side	NO (dimple)	6.44
4	Ir12	7.62	Left side	NO	6.22
5	Ir12	7.62	Left side	VOID	--------
6	Ir12	7.62	Left side	YES	4.66
7	Ir12	2.54	Left side	NO (dimple)	7.11
8	Ir12	2.54	Left side	YES (dimple)	3.77
9	Ir12	2.54	Right side	YES (dimple)	5.55
10	Ir12	2.54	Right side	YES	4
11	Ir12	2.54	Right side	YES	5.11
12	Ir12	2.54	Right side	YES(dimple)	3.77
13	Ir12	2.54	surface pons	YES	7.55
14	Ir12	2.54	surface pons	YES	4.66
15	Ir12	7.62	nerve root area	YES	2.66
16	Ir12	7.62	nerve root area	YES	2.22
17	Ir12	7.62	nerve root area	YES	1.55
18	Ir12	7.62	no specimen	calibration	1.55
19	Ir12	1.27	nerve root area	NO	7.11
20	Ir12	1.27	nerve root area	NO	6.22
21	Ir12	1.27	rostral VIII root	YES	3.55
22	Ir12	1.27	left side	NO (dimple)	4.44
23	Ir3	1.27	left side	NO (dimple)	6
24	Ir3	1.27	left side	YES (dimple)	6.22
25	Ir3	1.27	left side	NO	5.55
26	blunt needle	1.27	left side	NO (Calibration)	12
27	blunt needle	1.27	left side	NO (Calibration)	12

Table 4.1

Penetration Experiment #4 April 23, 1996

Insertion	Electrode type	velocity at impact cm/sec	Site of penetration	Penetration	Force in grams	Comments
1	SiIrMDX	7.62	left medulla	YES	2.5	Silicon probe peeled off
2	SiIrA(new)	7.62	left medulla	NO	2.5	Ir tip shaft ahead of dual shaft Silicon probe
3	SiIrA	7.62	left medulla	NO	3.8	same as above
4	SiIrA	7.62	left medulla	YES	5.5	Silicon probe broke off
5	SiIrA(new)	7.62	left medulla	NO	4.8	
6	SiIrA	7.62	left medulla	NO	6	
7	SiIrA	7.62	left medulla	NO	5	outrigger probe broke in half
8	SiIrA	7.62	left medulla	NO	4.8	broke rest of outrigger probe
9	SiIrA	7.62	left medulla	NO	5	Ir single shaft
10	Ir12(new)	7.62	left medulla	YES	1.5	full penetration
11	Ir12	7.62	left medulla	YES	1.5	full penetration
12	Ir12	7.62	left medulla	YES	1.3	full penetration
13	Ir12	2.54	left medulla	YES	1	full penetration
14	Ir12	2.54	right medulla	YES	1	full penetration
15	Ir12	2.54	through nerve root	NO	5	
16	4Ir12(new)	2.54	through nerve root	NO	4	4 shaft Ir w/staggered tips
17	4Ir12	2.54	through nerve root	NO	4	penetration after 150 msec of dimple
18	4Ir12	7.62	through nerve root	YES	10	static force observed - base
19	4Ir12	7.62	through nerve root	YES	5	static force observed - base
20	4Ir12	7.62	surface of pons	YES	4	full penetration

Table 4.2

Penetration Experiment #5 June 13, 1996

Insertions	Electrode type	velocity at impact cm/sec	Site of penetration	Penetration	Force in grams	Comments
1	SiIrE	2.54	medial to VIII	YES	1.55	little dimple
2	SiIrE	2.54	through VIII root	YES	0.88	little dimple
3	SiIrE	2.54	through VIII root	YES	1.55	little dimple
4	SiIrE	2.54	lateral to VIII	YES	3.30	little dimple
5	SiIrE	2.54	lateral to VIII	YES	1.77	little dimple
6	SiIrE	1.27	lateral to VIII	YES	1.33	full penetration
7	SiIrE	1.27	through VIII root	YES	2	full penetration
8	4Ir12	2.54	lateral to VIII (L)	YES	4.44	full penetration
9	4Ir12	7.62	lateral to VIII	YES	7.1	3/4 penetrated
10	4Ir12	7.62	through VIII root	YES	16.4	static force observed
11	4Ir12	7.62	through VIII root	incomplete	4.66	static force observed
12	4Ir12	7.62	lateral to VIII (L)	YES	3.11	static force observed
13	4Ir12	7.62	lateral to VIII	YES	3.77	full penetration
14	SiIrE(new)	1.27	through VIII root	YES	4.22	dimple
15	SiIrE	2.54	nerve root area	YES	14.88	large dimple
16	SiIrE	2.54	nerve root area	YES	13.11	two peaks observed
17	SiIrE	2.54	lateral to VIII	YES	2.22	clean penetration
18	SiIrE	2.54	lateral to VIII	YES	2.88	clean penetration

Table 4.3

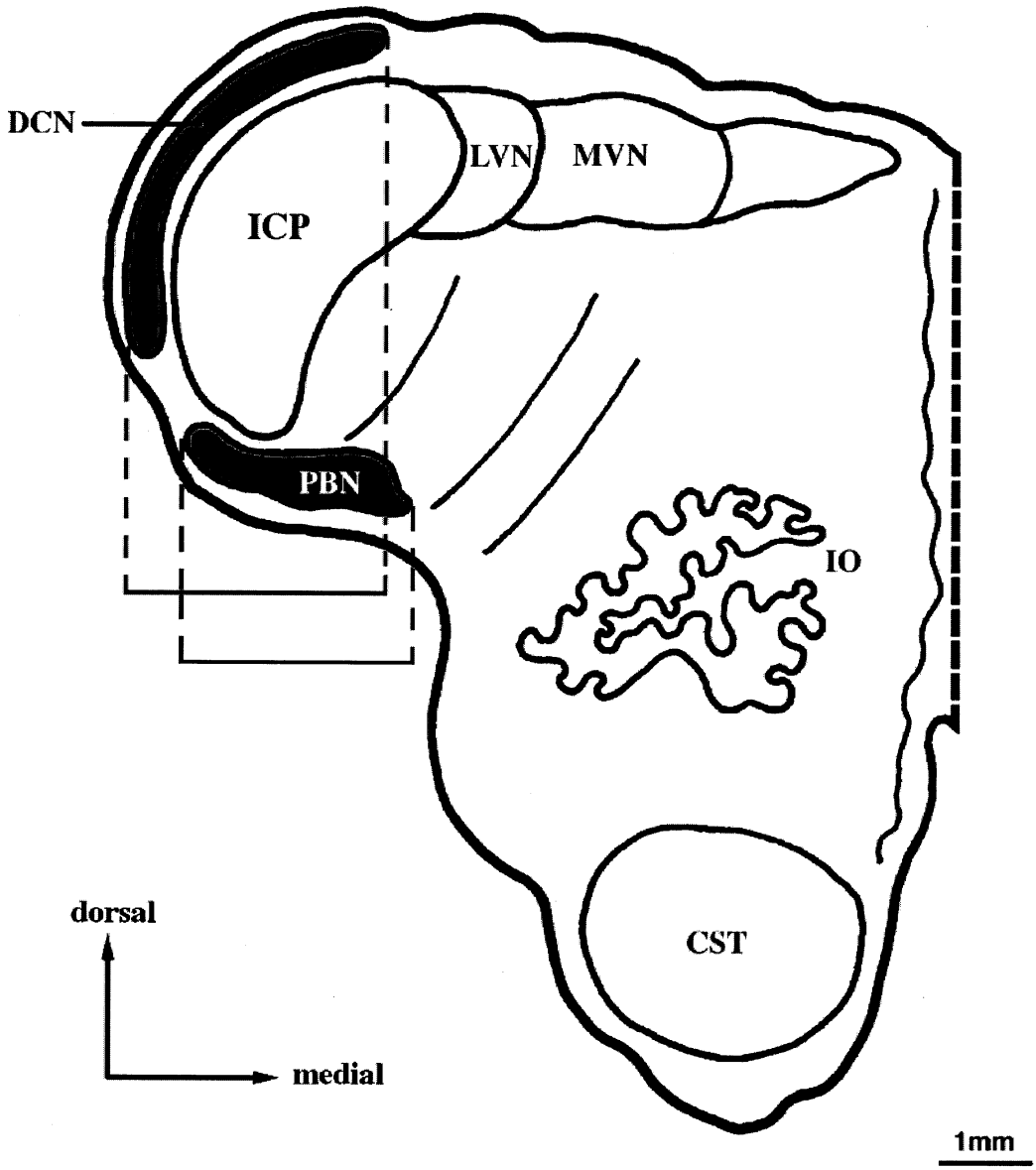

Fig. 2.1 Axial section through brainstem at level of DCN

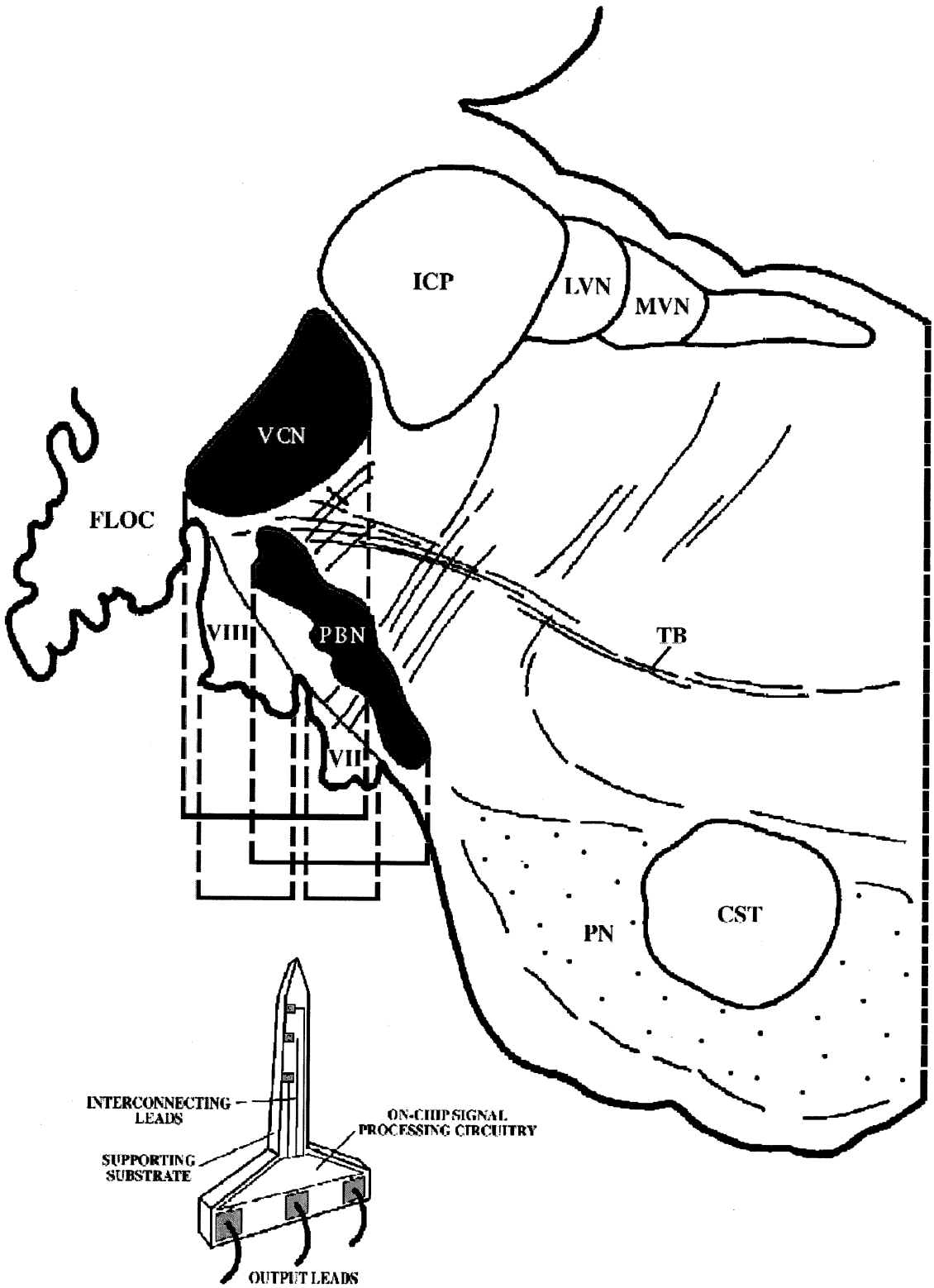

Fig. 2.2 Axial section through brainstem at level of VCN

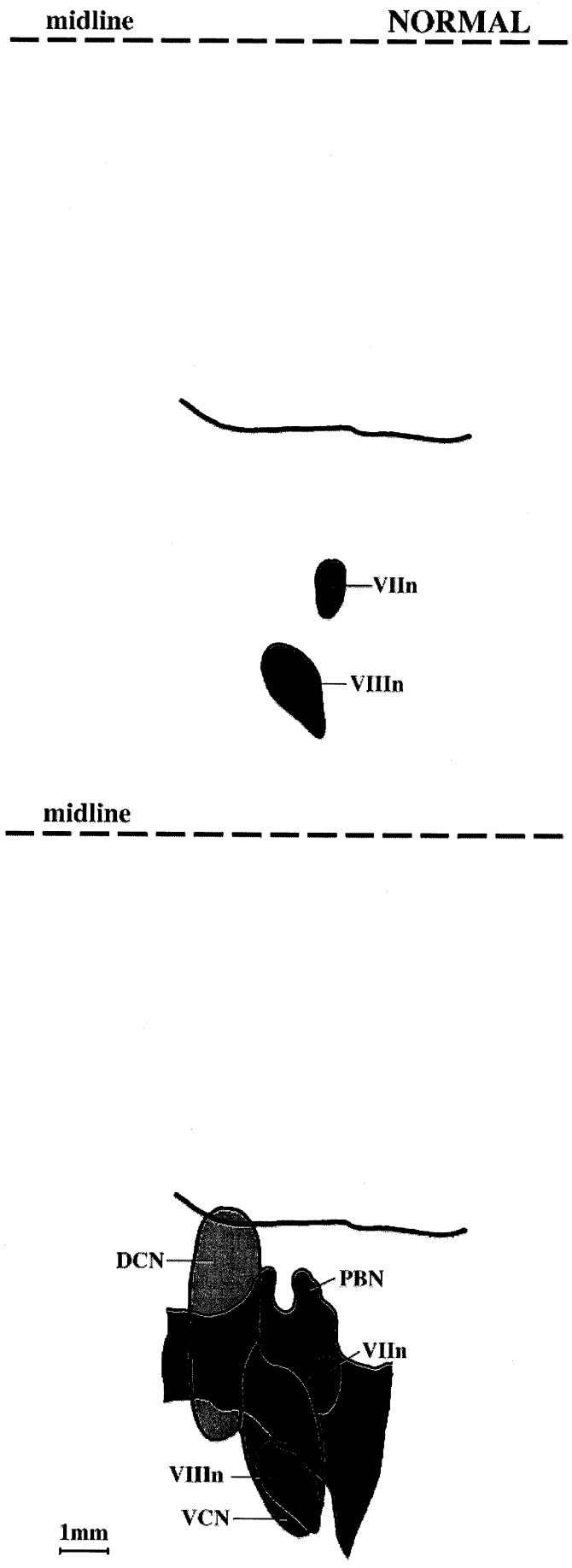

Fig. 2.3 Surface and deep structures in brainstem of a normal subject

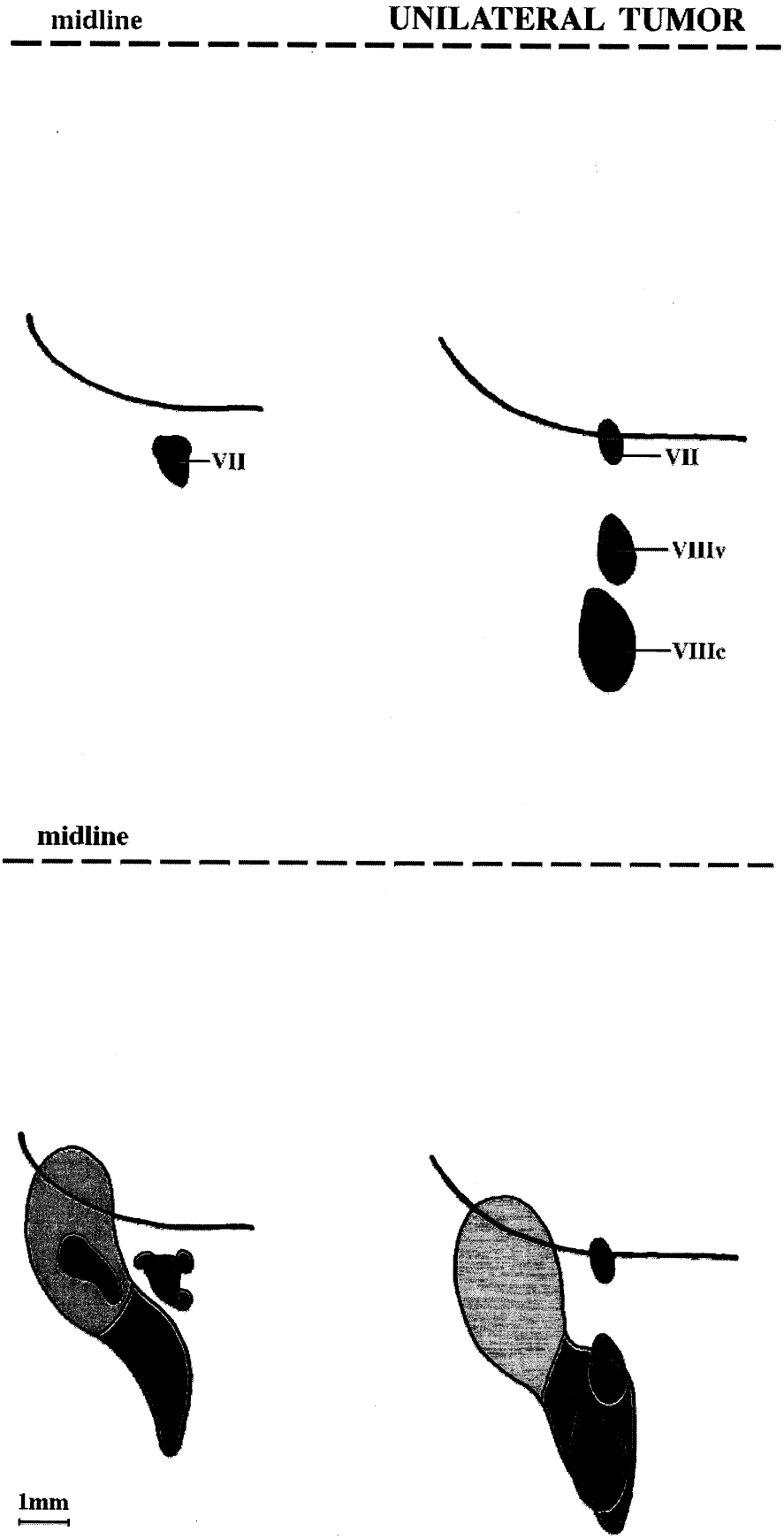

Fig. 2.4 Surface and deep structures in brainstems of unilateral neuroma subjects

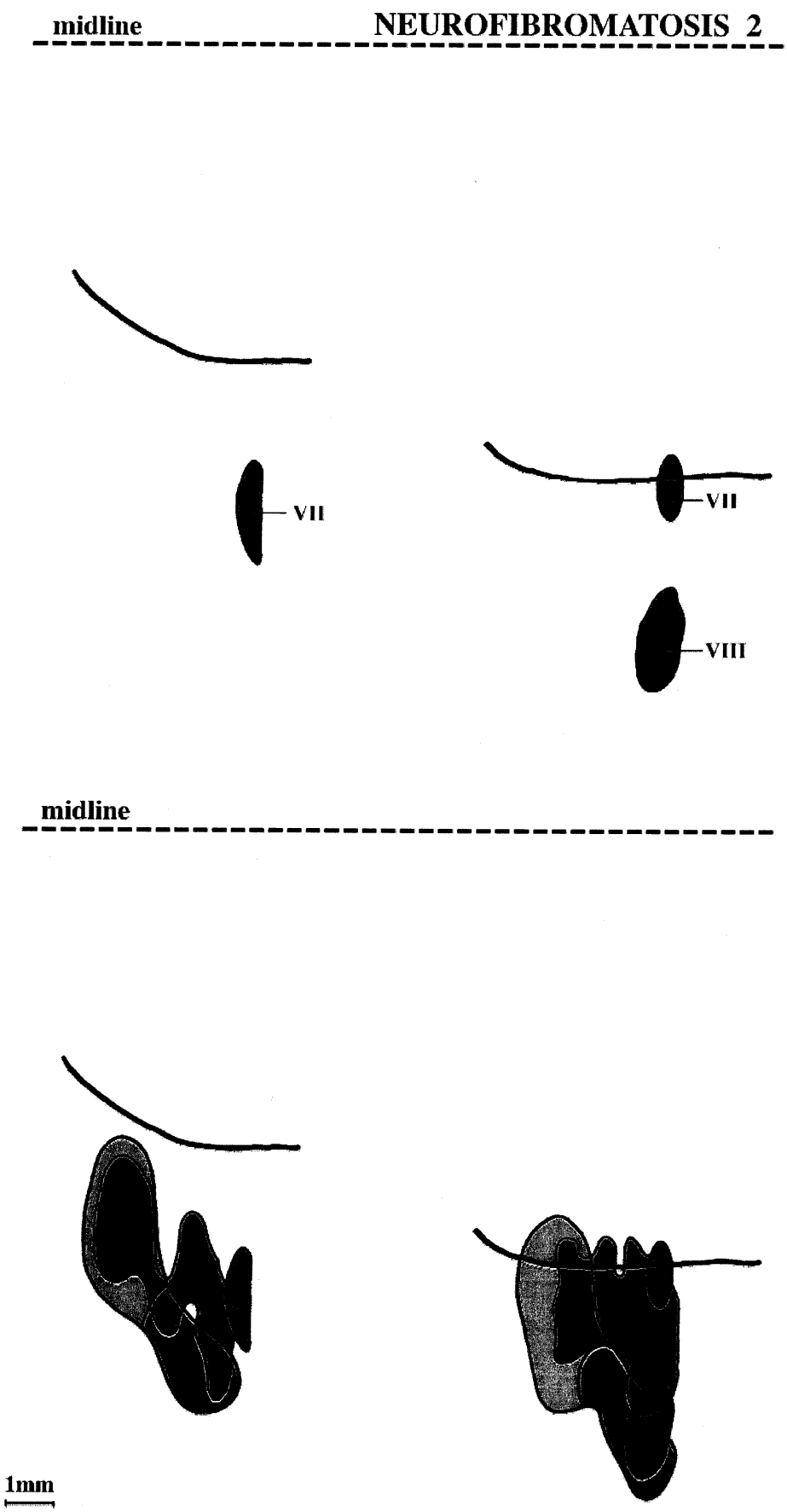

Fig. 2.5 Surface and deep structures in the brainstem of an NF2 subject

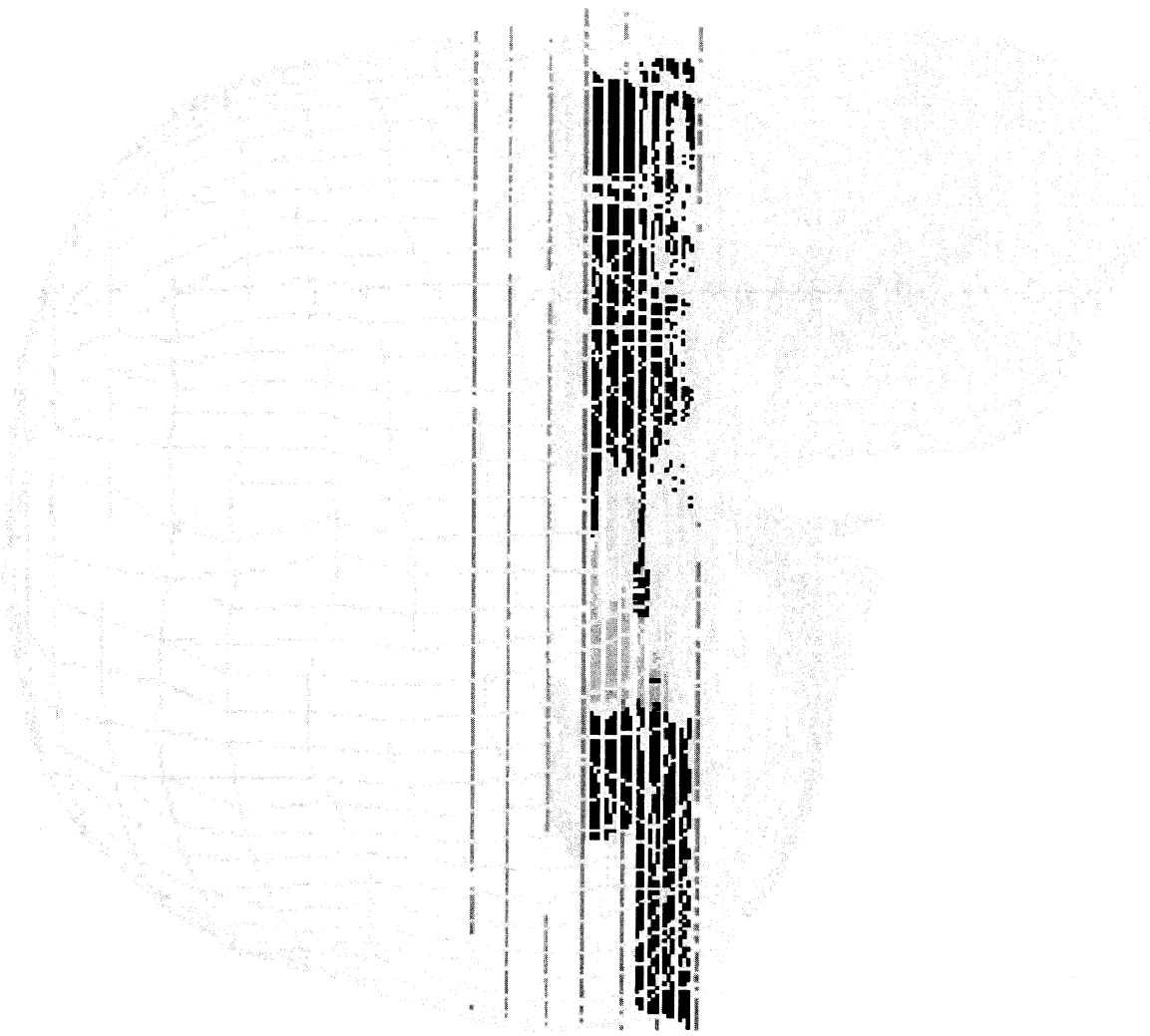

Fig. 3.1 CT images inserted into generic skull model

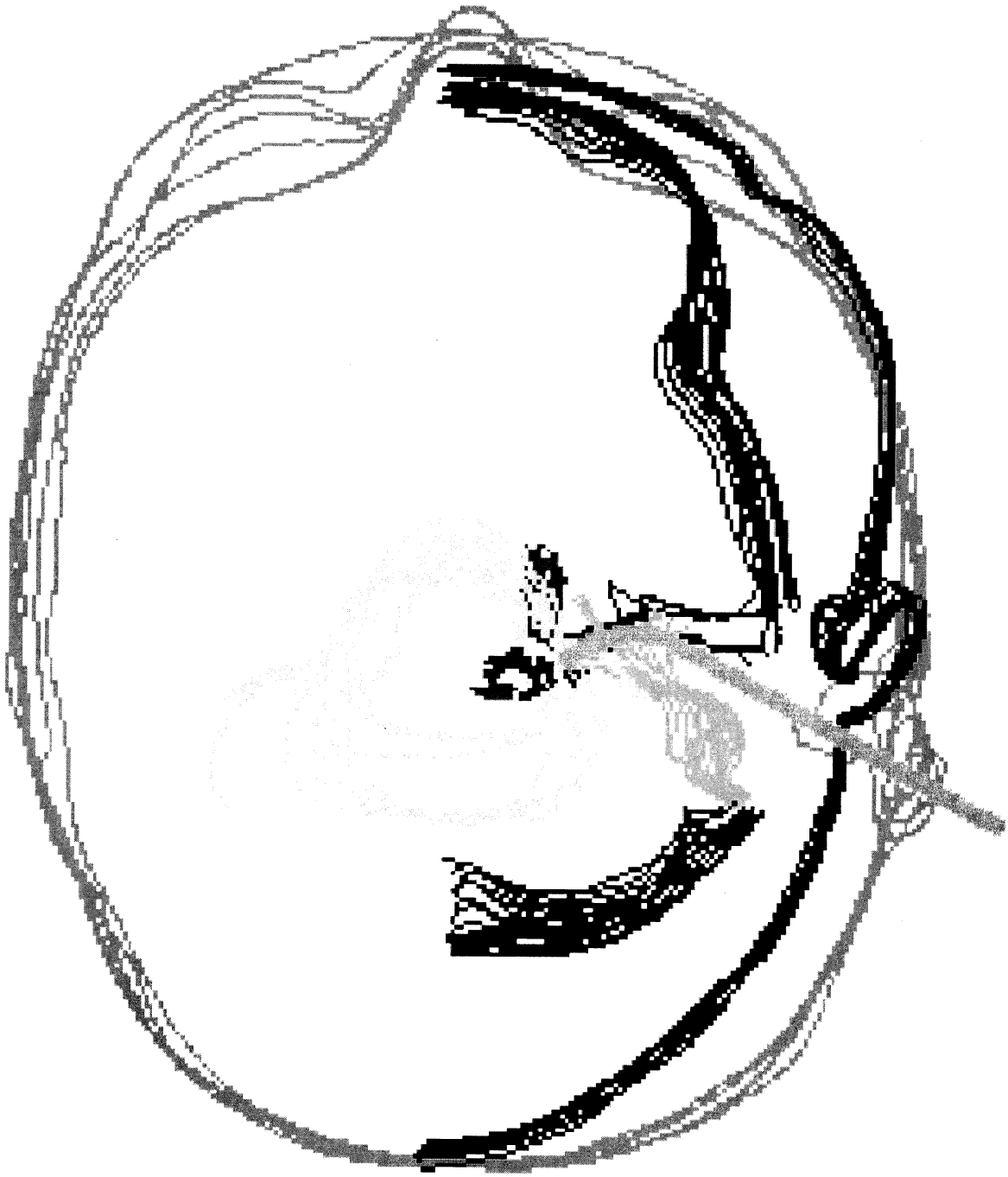

Fig. 3.2 Head and insertion tool in horizontal view

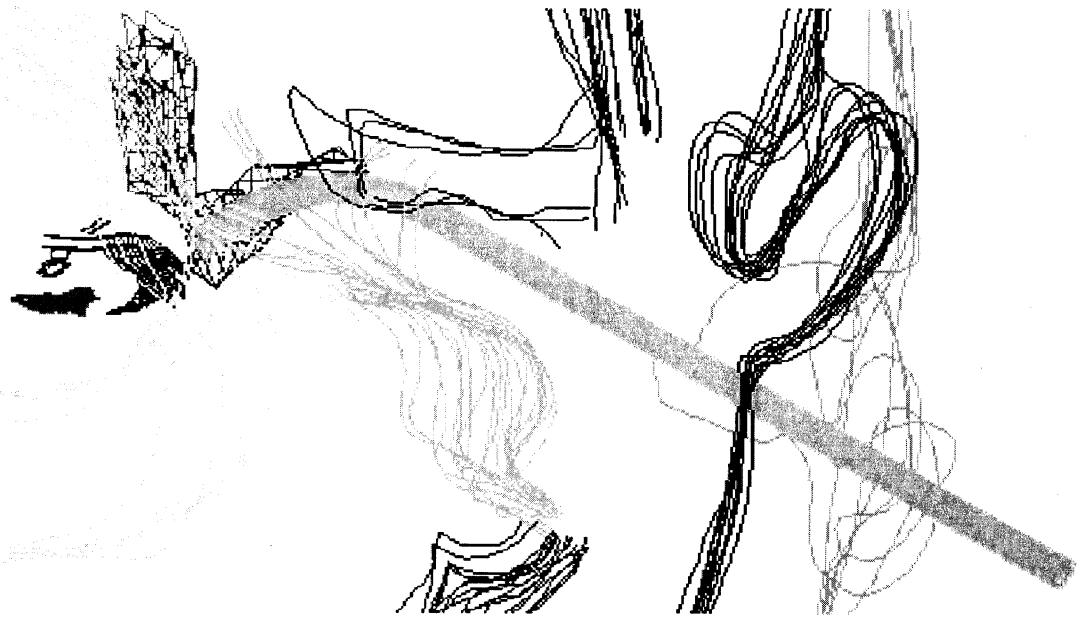

Fig. 3.3 Insertion tool and brainstem structures

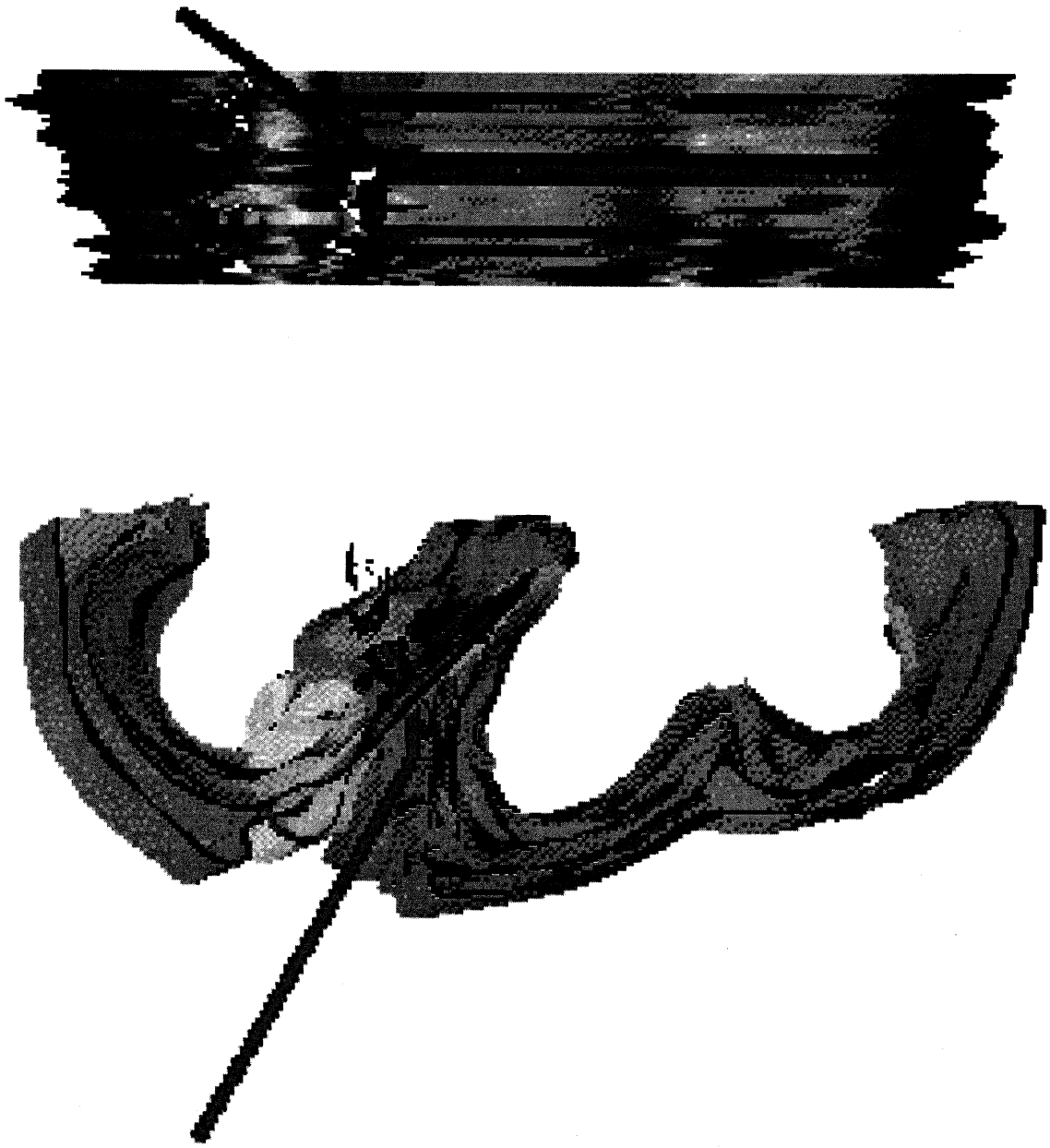

Fig. 3.4 Insertion tool and surgical access

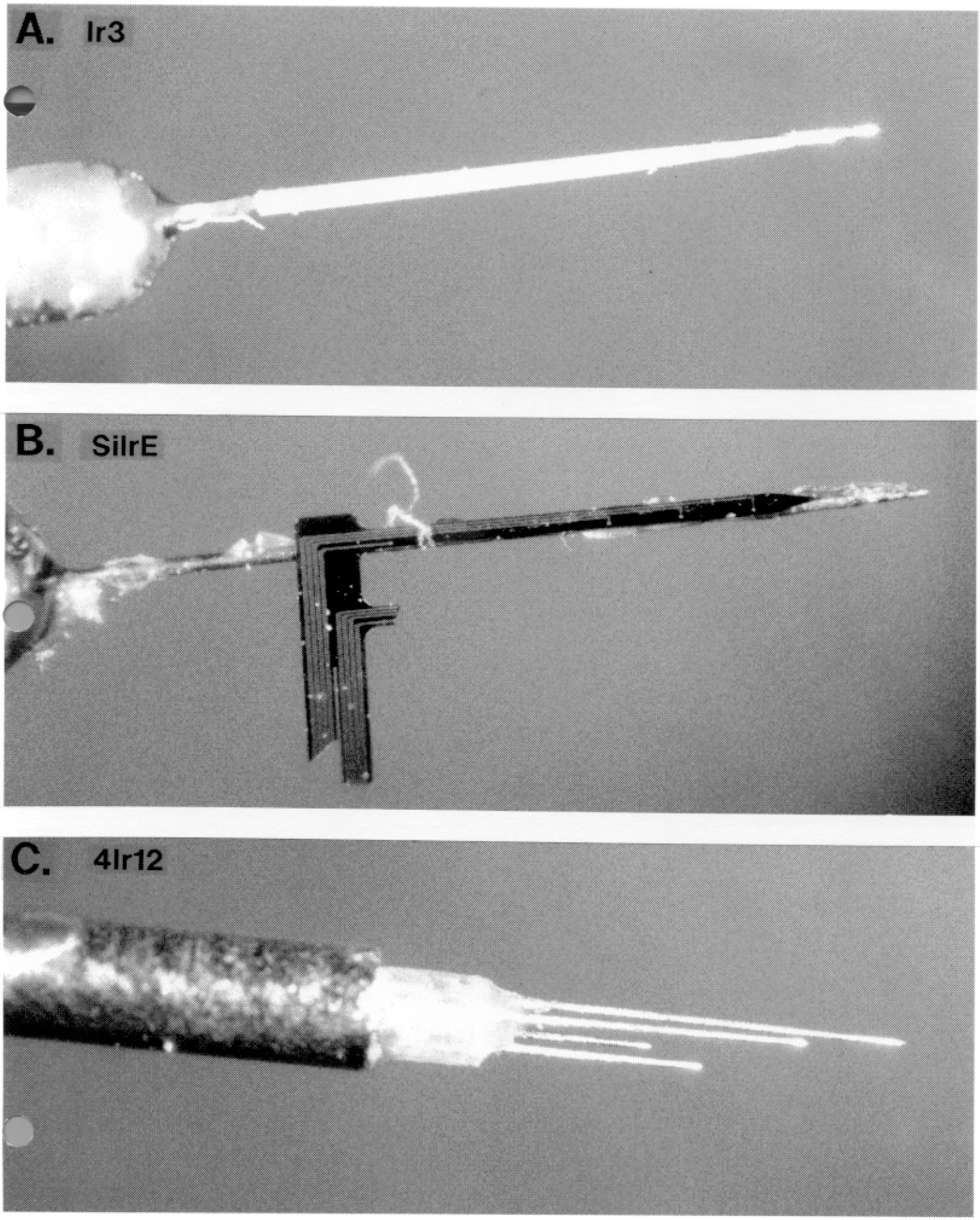

Fig. 4.1 Electrode types

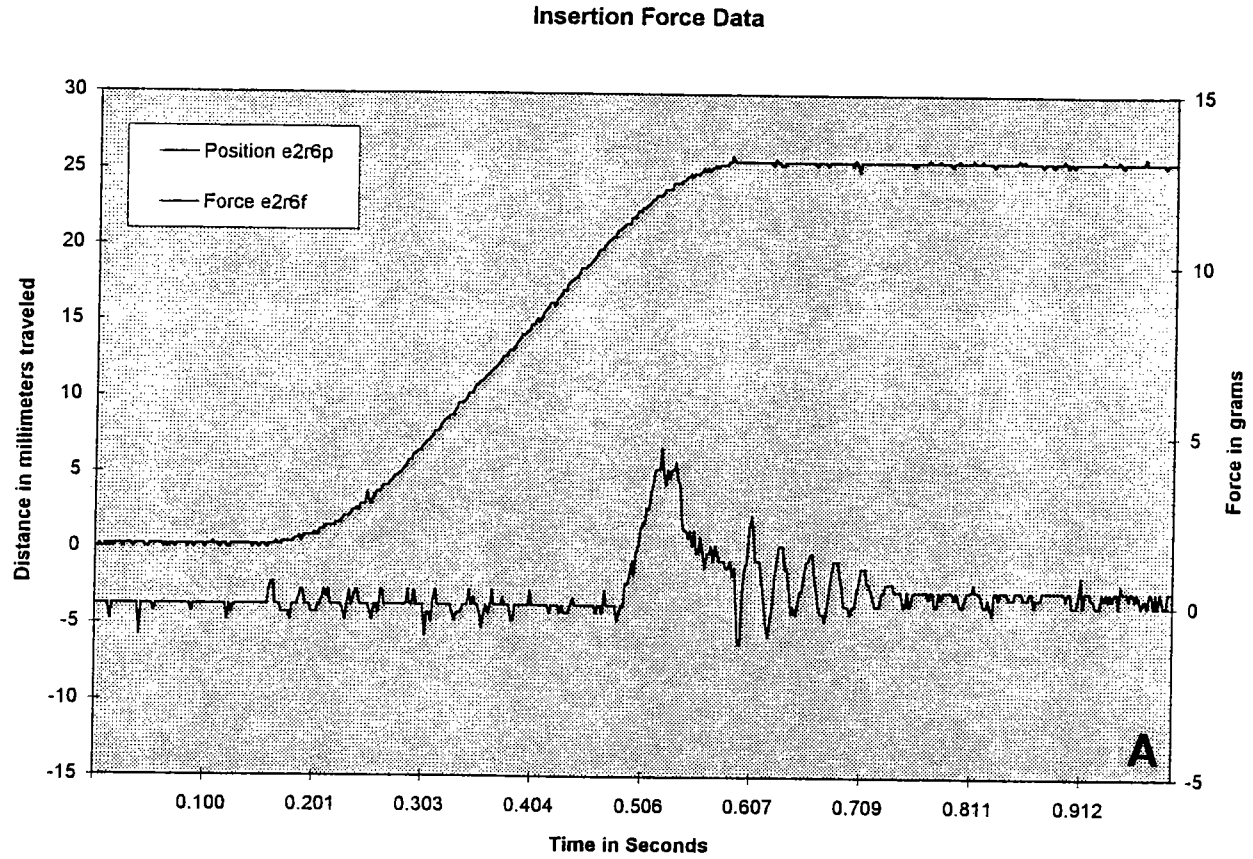

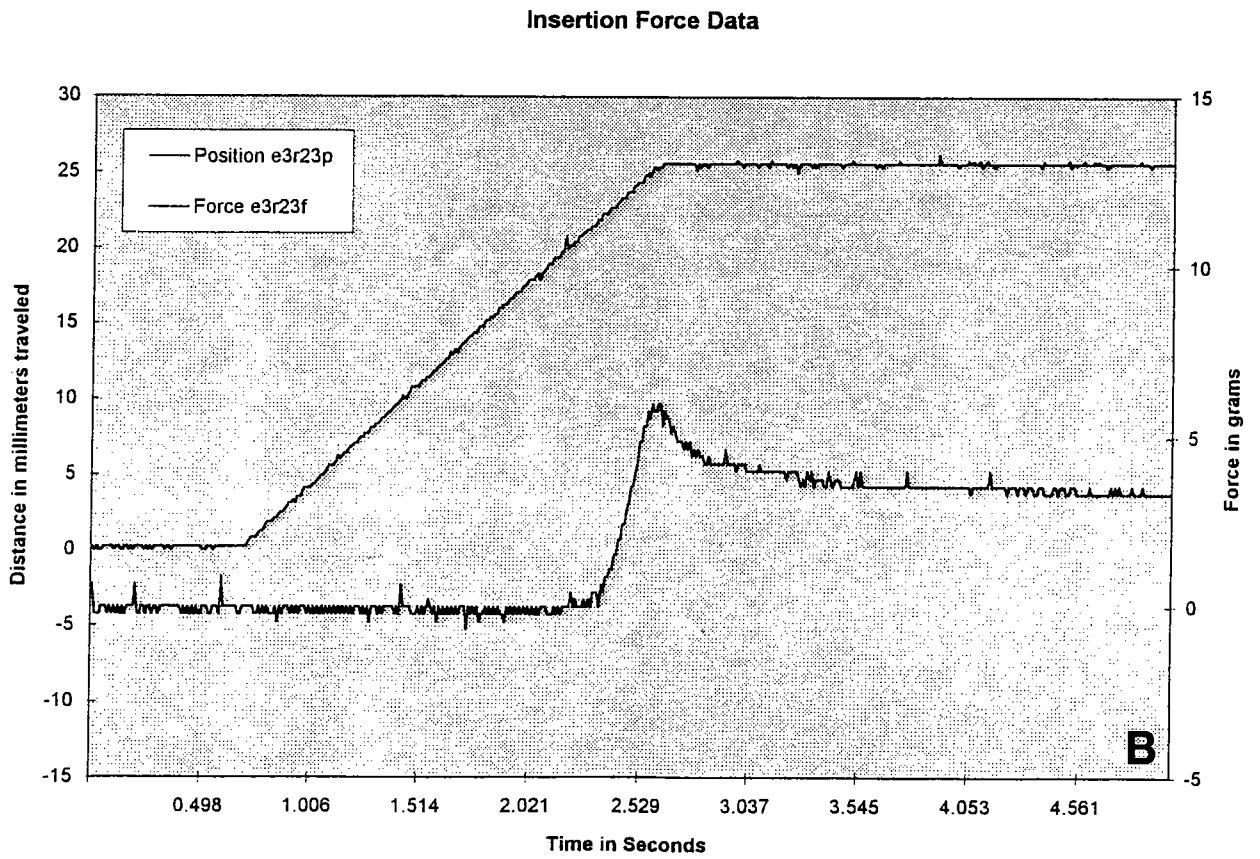

Fig. 4.2 Data from insertion force experiments

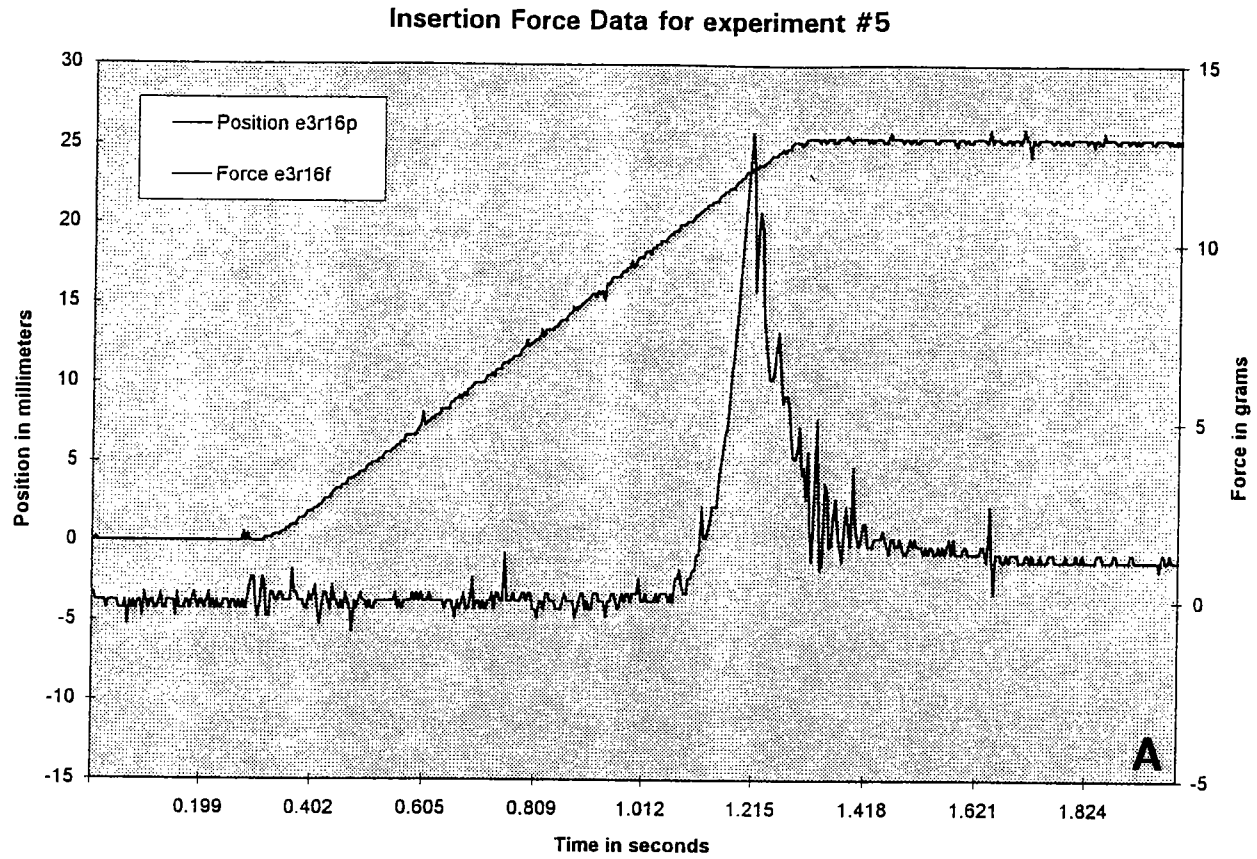

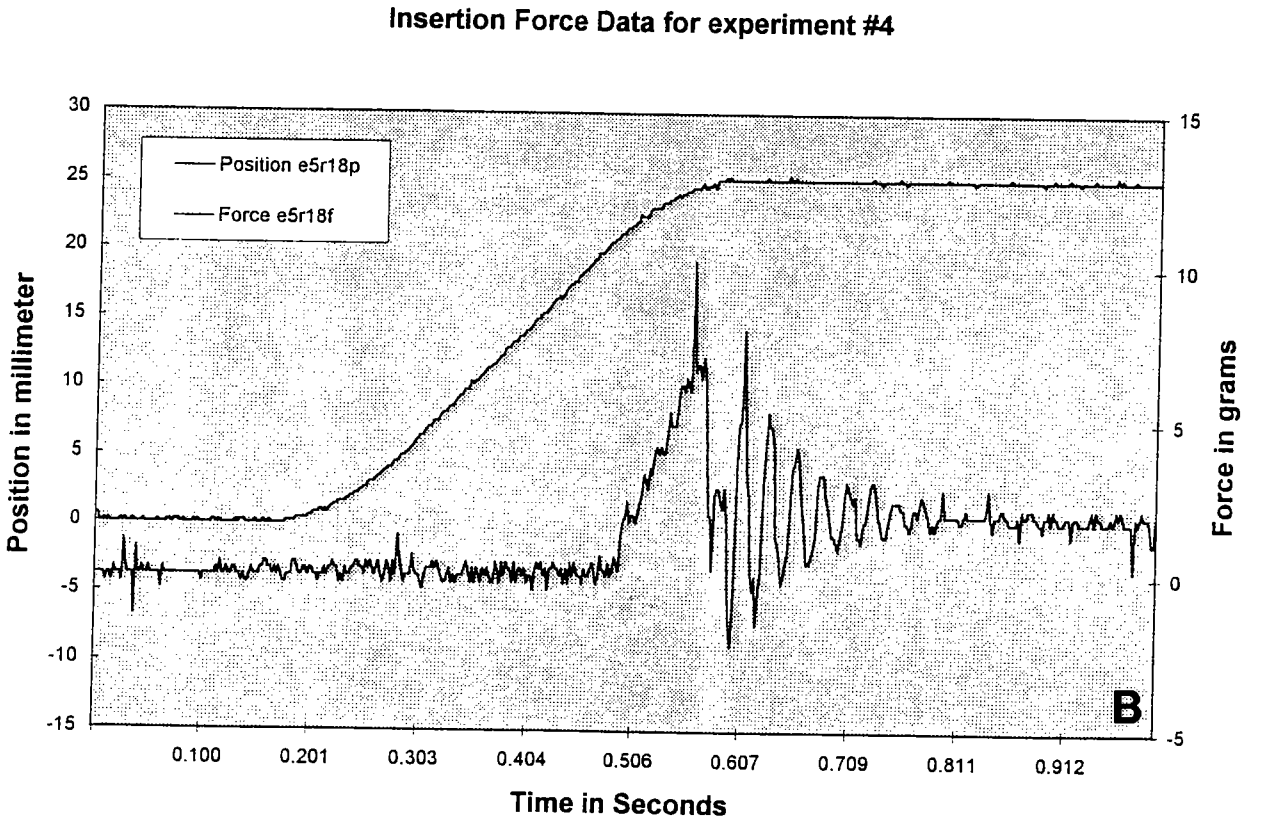

Fig. 4.3 Data from insertion force experiments